energies

MDPI

Article

Methane Storage Capacity of Permian Shales with Type III Kerogen in the Lower Yangtze Area, Eastern China

Lei Pan [1], Ling Chen [1,*], Peng Cheng [2] and Haifeng Gai [2]

[1] Guangxi Key Laboratory of Marine Disaster in the Beibu Gulf, Beibu Gulf University, Qinzhou 535011, China; panlei@bbgu.edu.cn
[2] State Key Laboratory of Organic Geochemistry, Guangzhou Institute of Geochemistry, Chinese Academy of Sciences, Guangzhou 510640, China; chengp@gig.ac.cn (P.C.); gaihf@gig.ac.cn (H.G.)
* Correspondence: cl@bbgu.edu.cn

Abstract: Marine–terrestrial transitional Permian shales occur throughout South China and have suitable geological and geochemical conditions for shale gas accumulation. However, the Permian shales have not made commercial exploitation, which causes uncertainly for future exploration. In this study, high-pressure methane (CH_4) adsorption experiments were carried out on the Permian shales in the Lower Yangtze area, and the influences of total organic carbon (TOC) content and temperature on adsorption parameters were investigated. The characteristics and main controlling factors of methane storage capacity (MSC) of the Permian shales are discussed. The results show that the maximum adsorption and the adsorbed phase density of these Permian samples are positively correlated with TOC contents but negatively correlated with temperatures. The pores of organic matter in shale, especially a large number of micropores and mesopores, can provide important sites for methane storage. Due to underdeveloped pore structure and poor connectivity, the methane adsorption capacities of the Permian shales are significantly lower than those of marine shales. Compared with the Longmaxi shales, the lower porosity and lower methane adsorption of the Permian shales are reasonable explanations for their lower gas-in-place (GIP) contents. It is not suitable to apply the index system of marine shales to the evaluation of marine–terrestrial transitional shales. The further exploration of Permian shales in the study area should be extended to overpressure stable reservoirs with high TOC contents (e.g., >5%), high porosity (e.g., >3%), and deep burial (e.g., >2000 m).

Keywords: high-pressure adsorption; methane storage capacity; marine–terrestrial transitional shale; type III kerogen; Permian

Citation: Pan, L.; Chen, L.; Cheng, P.; Gai, H. Methane Storage Capacity of Permian Shales with Type III Kerogen in the Lower Yangtze Area, Eastern China. *Energies* **2022**, *15*, 1875. https://doi.org/10.3390/en15051875

Academic Editor: Reza Rezaee

Received: 26 November 2021
Accepted: 31 January 2022
Published: 3 March 2022

1. Introduction

The predicted recoverable shale gas resources of the Yangtze Plate account for approximately 70% of the terrestrial resources of China [1], which occur in two sets marine shales (the Lower Silurian Longmaxi Formation and the Lower Cambrian Qiongzhusi Formation) and in the marine–terrestrial transitional Permian strata system [2–8]. Through the past decade of exploration and development, the marine shales in Sichuan Basin and its peripheral areas have been commercially exploited. Shale gas production reached 1.54×10^{10} m^3, with an increase of 41.3% in 2019, ranking third in the world [1,4]. However, the Permian shale in the Lower Yangtze area has not been commercially exploited. Only a few wells have conducted fracturing tests [9], and the gas contents of Permian shales were generally low, with on-site gas content between 0.22 and 2.1 m^3/t [10–12], which failed to meet the standard of the shale gas enrichment area, i.e., 2.5 m^3/t [13]. The industrial gas flow could not be obtained after hydraulic fracturing [9,10]. At present, the Permian shales still lack value for commercial exploitation.

There are many differences between the marine–terrestrial transitional shales and the marine shales in terms of gas generation, reservoirs, and preservation conditions [5–8].

In essence, it is mainly reflected in the different organic matter types. The marine shales are mainly composed of type I and/or type II kerogens [14–16], while the Permian shales are basically type III kerogen [17,18]. Compared with type I and type II kerogens, type III kerogen not only generates less oil and gas [19,20] but also affects the store space of shale system [21,22].

The Permian in the Lower Yangtze area is mainly composed of organic-rich shale, occurring in a large regional extent, and have moderate burial depths (generally 1000–4000 m) and large thicknesses (about 100–600 m), which are excellent geological conditions for shale gas generation and preservation [17,23–26]. According to a report by Pang et al. [1], the geological resources of shale gas in the study area can reach 8.92×10^{12} m^3, with a recoverable resource potential of 1.8×10^{12} m^3. The Permian shales are the key stratum for shale gas exploration and should have the potential to become the new growth point of shale gas reserves in the future. However, the exploration of Permian shales is still in the early stage. The number of drilling wells is very rare and is especially lacking in deep wells. Determining the next exploration direction has become an urgent scientific problem.

Shale gas in overmature shale is stored mainly as free gas and adsorbed gas, and the proportion of adsorbed gas can reach 20–85% [27–29]. High-pressure adsorption experiments are considered a common method to evaluate the adsorption capacity of shale and have been widely applied by many scholars [30–33]. At present, the previous studies mainly focused on the lower Paleozoic marine shales in the Upper Yangtze region. There is a lack of research on the MSC of marine–terrestrial transitional shales with type III kerogen. The relevant reports of the high-pressure adsorption of Permian shales are very limited [25], and it is difficult to accurately predict the GIP of Permian shales under geological conditions. In this context, systematic methane adsorption experiments were performed on the homologous Permian shales collected from relatively shallow reservoirs. Combining the experimental adsorption parameters with the set geological conditions of shale reservoirs, the MSC of Permian shales are evaluated and compared with marine shales. The purpose is to improve the evaluation of MSC of Permian shale, which will fill the gap of marine–terrestrial transitional shales. It is of great significance to clarify the next exploration direction of Permian shales in the Lower Yangtze area. In addition, the investigation of shale storage capacity is helpful to understand its potential as the carrier for CO_2 geological storage [34,35].

2. Geological Setting

The Lower Yangtze plate is bounded by the East China Sea and the Yellow Sea to the east and northeast, by the North China plate to the northwest, and by the South China plate to the south and southeast [36,37] (Figure 1). The sedimentary and tectonic movement includes three main stages [38]: marine sediments from the Early Paleozoic to the Middle Triassic, terrestrial sediments from the Late Triassic to the Early Cretaceous, and tectonic deformation and overprint from the Cretaceous to the Cenozoic. The initial marine sediments contain an alternating marine and terrestrial deposition (of Permian age) that was deposited along a continental margin [39,40]. During the Caledonian movement, the Yangtze plate was relatively stable and contained a large sedimentary thickness of 3000–10,000 m. The Indosinian and Himalayan movements carried out strong structural transformation on the strata, which led to an overall uplift of the Lower Yangtze plate and extensive erosion of Mesozoic strata [39]. The thickness of organic-rich Permian shales ranges from 100 to 600 m, with an average TOC content greater than 2% and occasionally reaching 21% [17,23].

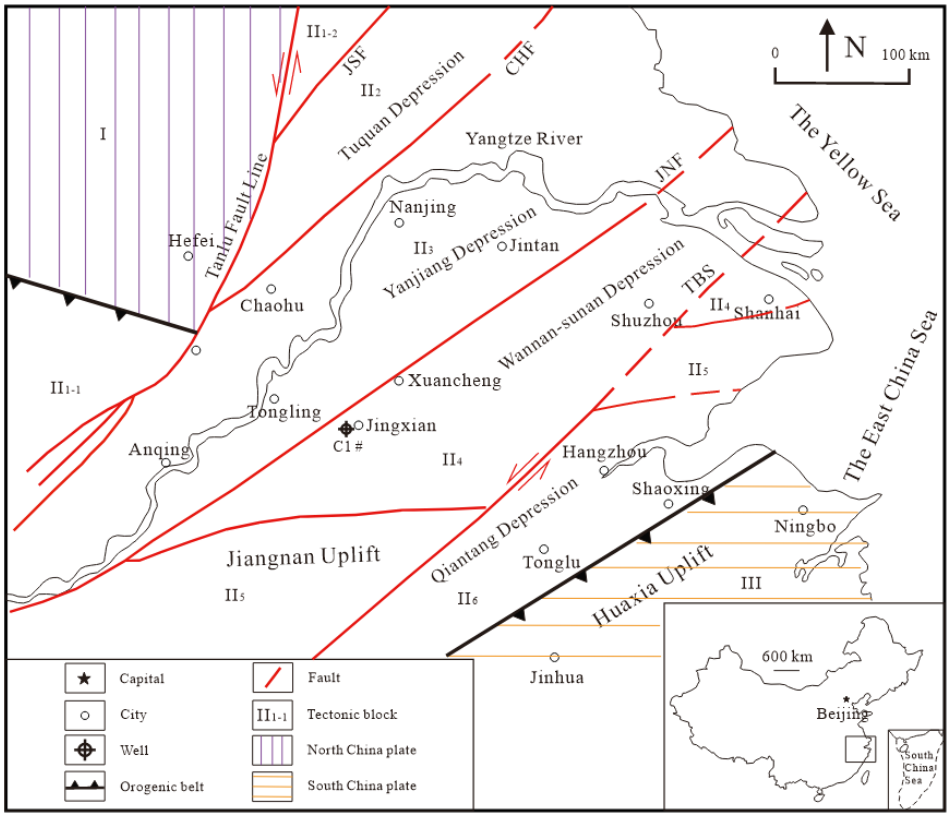

Figure 1. The tectonic location diagram of the Lower Yangtze area and sampling location (modified from Zhu et al. [37]). JSF: Jiashan-xiangshui Fault; CHF: Chuhe Fault; JNF: Jiangnan Fault; TBS: Tianmushan-baijishan Shear Zone.

3. Samples and Methods

3.1. Samples

The Permian shale samples were collected from well C1 (Figure 1), which is located at Wuhu block in the Lower Yangtze area. Their geochemistry parameters, mineralogical compositions, and pore structural characteristics were reported by Pan et al. [17] (Table 1). Briefly, the selected samples cover a wide range of TOC contents, varying from 0.94% to 11.80%, with an average vitrinite reflectance (Ro) value of 2.34–2.58%. The samples are rich in quartz ranging from 30.5% to 86.3%, and clay minerals ranging from 11.3% to 59.4%. The contents of carbonate and feldspar are 0–21.8% and 0–21.2%, respectively. Their total porosity varies from 1.96% to 4.65%. The Brunauer–Emmett–Teller (BET) surface area and micropore volumes are in the range of 9.61–19.77 m^2/g rock and 0.38–0.80 $cm^3/100$ g rock, respectively.

3.2. FE-SEM Observations

Field emission scanning electron microscopy (FE-SEM) observations were performed on polished shale surfaces. An observation surface with a larger area and higher quality can be obtained by multistage Ar ion milling with different acceleration voltages. First, the acceleration voltage was set at 6 kV with a milling time of 4 h, and then reduced to 3 kV with a milling time of 1 h. Secondary electron (SE) images were acquired by the upper detector on the Hitachi SU8010 system. Due to the poor conductivity of shale, lower accelerating voltages (1–2 kV) with small working distances (2–4 mm) were set to prevent beam damage of shale samples and ensure high-definition images. These images can provide important information on compositional variations and the types and sizes of pores [15,41].

Table 1. Geochemistry parameters, mineralogical compositions and pore structure characteristics of the Permian samples (data from Pan et al. [17]).

Sample	Depth	TOC	Ro	Porosity	V_{mic}	S_{BET}	Mineralogical Compositions Relative Percent (%)				
	(m)	(wt.%)	(%)	(%)	$cm^3/100$ g	(m^2/g)	Quartz	Feldspar	Clays [1]	Carbonate [2]	Other [3]
C1-1	123.4	9.95	2.34	3.59	0.79	17.91	62.2	21.2	11.3	0	5.3
C1-4	261.9	1.36	2.44	2.09	0.38	9.61	30.5	10.9	58.6	0	0
C1-5	288.0	0.94	Nd [4]	1.96	0.39	10.09	34.8	5.80	59.4	0	0
C1-7	326.3	11.8	2.51	4.65	0.80	18.24	86.6	0	12.7	0	1
C1-9	337.2	6.18	2.58	2.29	0.47	14.08	45.2	0	34.9	18.0	1.9
C1-10	341.8	8.83	2.55	2.97	0.66	19.77	32.0	0	37.3	21.8	8.9

[1] Clays = illite + chlorite. [2] Carbonate = Calcite + Dolomite. [3] Others = Pyrite + Siderite. [4] Nd = No data.

3.3. High-Pressure Methane Adsorption Experiments

The Permian shale samples were dried in a vacuum at 60 °C for 24 h and then were crushed and sieved for an 80 to 40 mesh (380 to 180 μm) size fraction. The selected parts were dried again in a vacuum at 110 °C for 24 h. The ISOSORP-HP Static II model with magnetic levitation balance was used for high-pressure adsorption measurements. The precision of the balance was 0.01 mg, and the measurable values of temperature and pressure reached 40–200 °C and 0–35 MPa, respectively. The sample container was wrapped by a heating oil bath cycle with an accuracy of 0.01 °C. The excess adsorption amount was directly measured, and then calculated by a blank and buoyancy corrections [8,14,42]. The experimental adsorption temperature was set at 60 °C for all samples. Five extra temperatures (40, 80, 100, 120 and 150 °C) were measured for three selected samples (C1-4, C1-7 and C1-10).

3.4. Adsorption Parameters of Shale

3.4.1. Calculation of Adsorption Gas

According to the Gibbs adsorption [43–46], the relationship between excess adsorption and absolute adsorption can be expressed by the following equation:

$$n_{ex} = n_{ab} \cdot \left(1 - \frac{\rho_b}{\rho_{ad}}\right) \quad (1)$$

where n_{ab} represents the absolute adsorption, n_{ex} represents the excess adsorption, ρ_b is the gas phase density, and ρ_{ad} is the adsorbed phase density.

At present, the Langmuir model is widely used to characterize the adsorption characteristics of porous media, such as activated carbon, coal, and shale [3,7,47]. The supercritical Dubinin–Radushkevich (SDR) model is used to characterize the high-pressure adsorption under supercritical conditions, which is modified from the classical Dubinin–Radushkevich (DR) equation for subcritical adsorption [31,48–50]. The SDR model is more reasonable than the Langmuir model, because the density of adsorbed methane fitted by the SDR model is less than the liquid density of methane at its boiling point [7,8,31]. Therefore, the SDR model is selected and takes the following form:

$$n_{ex} = n_0 \cdot \exp\left\{-D \cdot \left(ln\left(\frac{\rho_{ad}}{\rho_b}\right) \cdot RT\right)^2\right\} \cdot \left(1 - \frac{\rho_b}{\rho_{ad}}\right) \quad (2)$$

where n_0 represents the maximum absolute adsorption, D is an interaction constant related to pore structure [51], T is the Kelvin temperature, and R is the ideal gas constant.

3.4.2. Calculation of Adsorbed Gas, Free Gas, and Total Gas

Pan et al. [8] proposed a method to calculate adsorbed gas, free gas, and total gas content at different burial depths. The adsorbed gas and total gas can be calculated by excess adsorption, while the free gas is equal to the total gas minus the adsorbed gas. The total gas content is expressed using the sum of excess adsorption and free gas corresponding

to the rest volume. The adsorbed gas, total gas, and free gas at specific geological conditions can be calculated using the following equations, respectively:

$$n_{ab}^{H} = \frac{n_{ex}^{H} \cdot \rho_{ad}^{H}}{\rho_{ad}^{H} - \rho_{b}^{(H,T,y)}} \tag{3}$$

$$n_{total}^{H} = n_{ex}^{H} + \frac{\varphi \cdot (1 - S_w)}{\rho_a} \cdot \frac{\rho_{b}^{(H,T,y)}}{\rho_{b}^{\mathrm{STP}}} \tag{4}$$

$$n_{free}^{H} = n_{total}^{H} - n_{ab}^{H} \tag{5}$$

where n_{ex}^{H}, n_{ab}^{H}, n_{free}^{H}, n_{total}^{H}, ρ_{ad}^{H}, and $\rho_{b}^{(H,T,y)}$ are the excess adsorbed gas, absolute adsorbed gas, free gas, total gas, adsorbed phase density, and bulk gas phase density at a burial depth of H, respectively. φ is the total porosity, S_w is the water saturation, ρ_a is the apparent density of shale, and ρ_{b}^{STP} represents the density of methane at standard temperature and pressure conditions.

3.5. Thermodynamics of Methane Adsorption

The required equilibrium pressure (P) is related to the temperature (T) for a given adsorption (n). Their relationship can be expressed as the following equation [52]:

$$\ln(P)_n = -\frac{Q_{st}}{R \cdot T} + \left(\ln P^0 - \frac{\Delta S^0}{R} \right) \tag{6}$$

where Q_{st} is the isosteric heat, P^0 represents the standard atmospheric pressure, and ΔS^0 is the standard entropy. Q_{st} and ΔS^0 were determined from the slope and intercept of the regression line on the plot of the natural logarithm pressure versus the reciprocal of the Kelvin temperature [53].

4. Results and Discussion

4.1. Isothermal Adsorption Curve

The excess adsorptions were directly measured (Figure 2a), and the adsorption parameters were fitted by the SDR model [8,31,48]. The absolute adsorptions were constructed by measuring and fitting adsorption parameters (Figure 2b). The measured maximum excess adsorption varies from 0.72 cm^3/g rock to 2.08 cm^3/g rock, while the fitted maximum absolute adsorption varies from 1.11 cm^3/g rock to 3.17 cm^3/g rock (Table 2). The excess adsorption curves increase rapidly at first and then decrease with increasing pressure, with a maximum corresponding to pressures between 9 and 13 MPa. It will be reduced to zero when the bulk methane density is equal to the adsorbed phase density if the experimental pressure continues to increase. The shape of the absolute adsorption curves is similar with the type I adsorption curve defined by IUPAC [54]. The difference between excess adsorption and absolute adsorption gradually increases with increasing pressure.

The adsorption isothermal curves of three selected samples (C1-4, C1-7 and C1-10) at different temperatures also have obvious differences (Figure 3). With an increase in temperature, the excess adsorption decreases in the experimental pressure range (0–35 MPa), and the pressure corresponding to the maximum excess adsorption increases slightly (Figure 3a,c,e). The higher the temperature is, the lower the absolute adsorbed amount (Figure 3b,d,f) because the adsorption of methane in shale is an exothermic process [55,56] and it does not change with the type of kerogens [7,14,31,53]. Therefore, these adsorption isothermal curves on marine–terrestrial transitional shales with type III kerogen are basically consistent with those of marine shales with type I or type II kerogen [7,8,14,31].

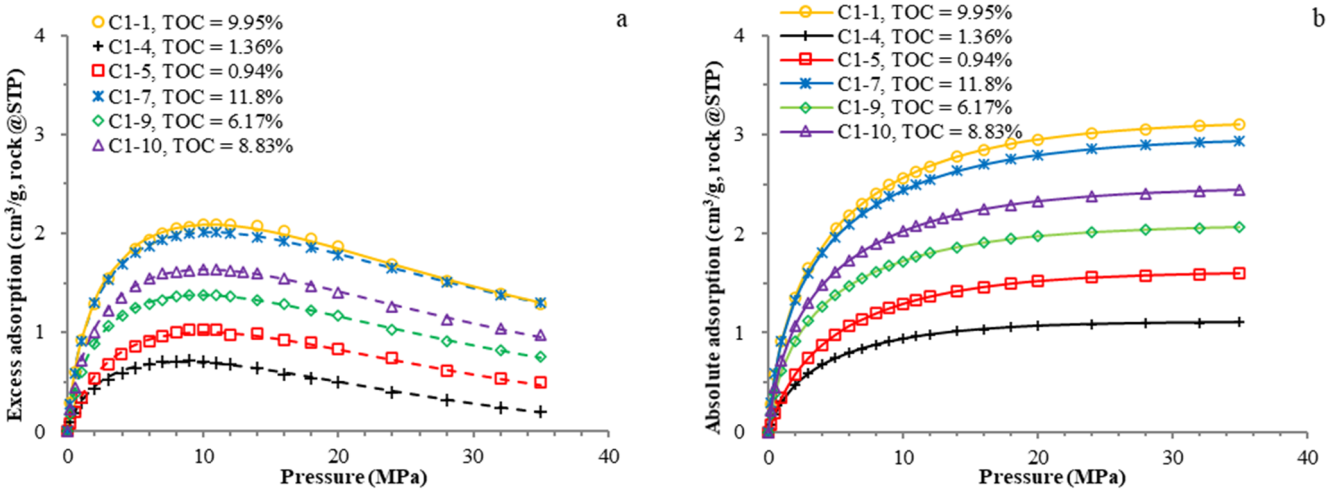

Figure 2. Measured and fitted methane excess adsorption isotherms (**a**) and calculated absolute adsorption isotherms using the SDR model (**b**) for the studied Permian samples at 60 °C.

Table 2. Adsorption parameters of the studied samples fitted by SDR model at 60 °C.

Sample	n_{ex}^{max} (cm³/g) [1]	Pressure (MPa)	n_{ab}^{max} (cm³/g) [1]	D (mol²/KJ²)	ρ_{ad} (g/cm³)	V_{ad} (cm³/100 g)
C1-1	2.08	~10	3.17	0.0097	0.347	0.65
C1-4	0.72	~9	1.11	0.0121	0.243	0.33
C1-5	1.03	~11	1.60	0.0132	0.282	0.41
C1-7	2.02	~10	3.01	0.0091	0.360	0.60
C1-9	1.37	~9	2.11	0.0100	0.314	0.48
C1-10	1.64	~11	2.49	0.0110	0.327	0.54

[1] 1 mmol/g = 16 mg/g = 22.4 cm³/g rock @STP.

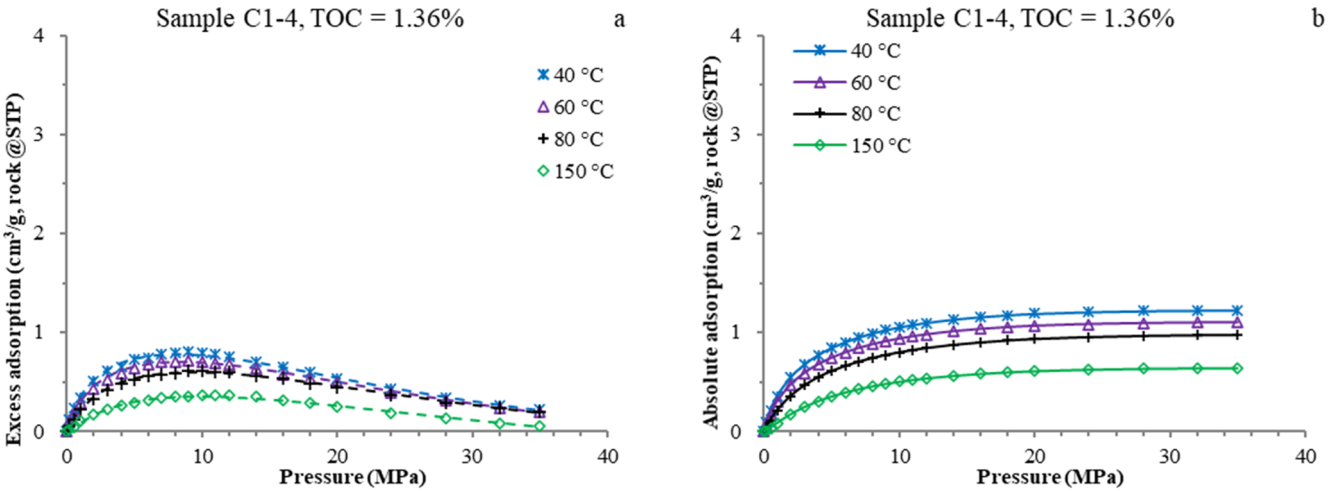

Figure 3. *Cont.*

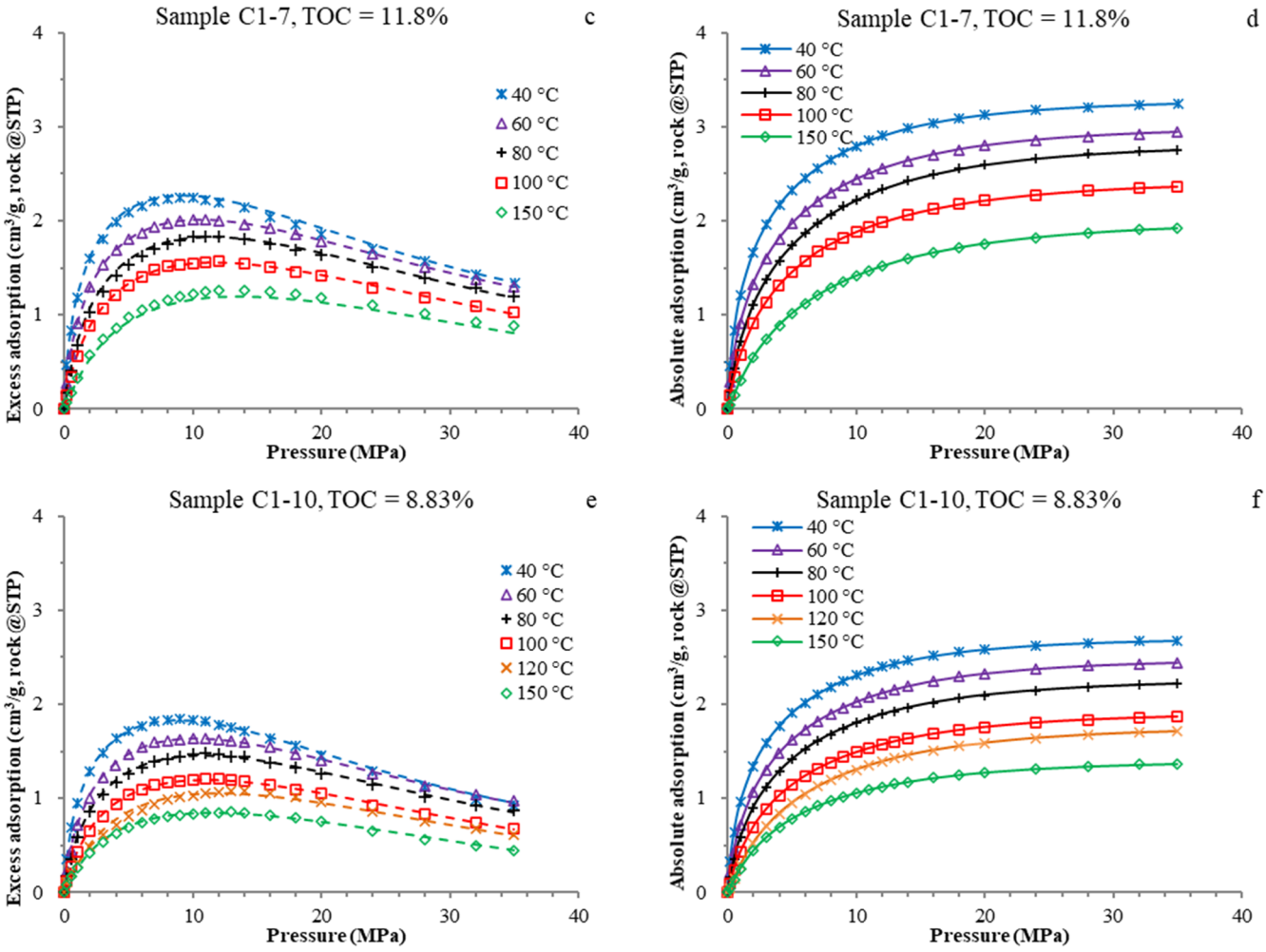

Figure 3. Measured and fitted excess adsorption isotherms against equilibrium pressure (**a**,**c**,**e**) and their absolute adsorption isotherms calculated by the SDR model (**b**,**d**,**f**) at various temperatures for the three selected samples.

4.2. Influence of TOC Content on Adsorption Characteristics

There are linear positive correlations between the maximum adsorbed amounts with TOC content (Figure 4, Table 3), which implies that the organic matter can provide storage sites for methane adsorption in shale [3,6,32]. The maximum excess and absolute adsorption amount for a sample without organic matter (i.e., TOC = 0%) is 0.73 cm^3/g rock and 1.15 cm^3/g rock, respectively. Ji et al. [57] reported that the clay minerals in shale could also contribute a portion of methane adsorption capacity. Especially for the samples with low TOC content, the contribution of clay minerals should be dominant [58]. However, the contribution of organic matter increases significantly with increasing TOC content (Figure 4).

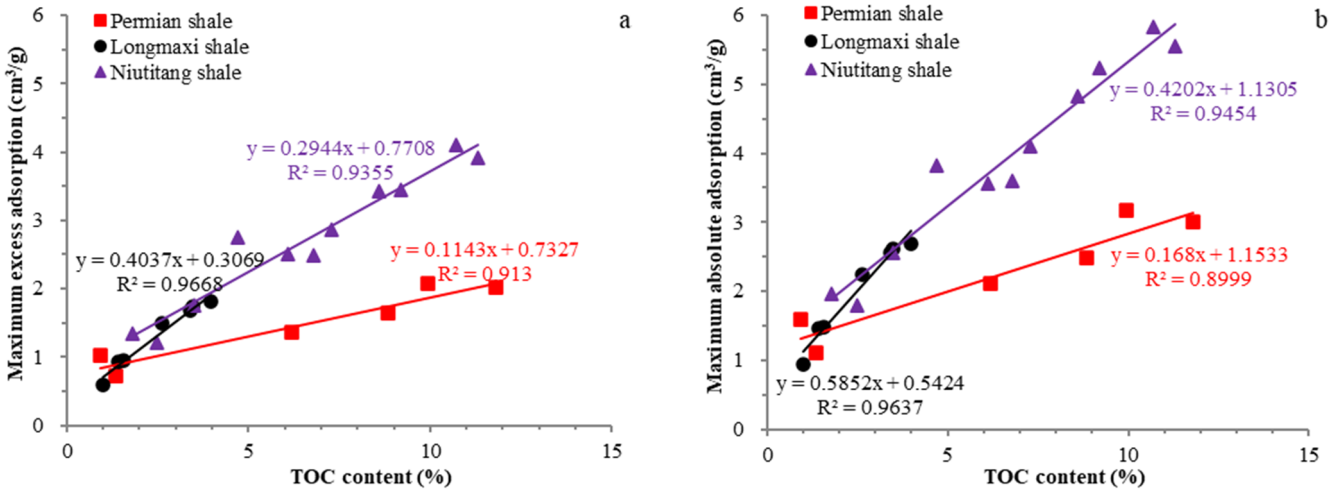

Figure 4. Plots showing the relationships between the maximum excess adsorption with the TOC content (**a**) and the maximum absolute adsorption with the TOC content (**b**). (The adsorption temperature is 60 °C and the Longmaxi and Niutitang shales are from Pan et al. [8] and Li et al. [14], respectively).

Table 3. Pearson correlation analysis between adsorption parameters and reservoir physical properties of the studied samples.

	TOC	Clay	Porosity	S_{BET}	V_{mic}	n_{ex}^{max}	n_{ab}^{max}	ρ_{ad}	V_{ad}
Clay	−0.946 **								
Porosity	0.904 *	−0.886 *							
S_{BET}	0.944 **	−0.819 *	0.769						
V_{mic}	0.957 **	−0.936 **	0.934 **	0.902 *					
n_{ex}^{max}	0.956 **	−0.96 **	0.873 *	0.900 *	0.967 **				
n_{ab}^{max}	0.949 **	−0.958 **	0.859 *	0.896 *	0.961 **	1.000 **			
ρ_{ad}	0.946 **	−0.926 **	0.848 *	0.891 *	0.914 **	0.978 **	0.977 **		
V_{ad}	0.930 **	−0.946 **	0.826 *	0.890 *	0.951 **	0.995 **	0.997 **	0.965 **	
D	−0.957 **	0.906 *	−0.792	−0.891 *	−0.849 *	−0.862 *	−0.856 *	−0.859 *	−0.835 *

**: $p < 0.01$, *: $p < 0.05$, n = 6.

The adsorption data of the Lower Silurian and Lower Cambrian shales in the Upper Yangtze area with the same experimental temperature (60 °C) are compared with those of the Permian shales in the Lower Yangtze area [8,14] (Figure 4). When the TOC content exceeds 2%, the maximum adsorptions of the Permian shales are significantly lower than those of the Lower Silurian and Lower Cambrian shales. In addition, the regression line of Permian shales in Figure 4b has a slope of 0.168, indicating an absolute adsorption capacity of organic matters of 16.8 cm^3/g TOC. This value is lower than these values of marine shales, e.g., 42–58 cm^3/g TOC. The contribution of unit organic matter to the adsorption capacity of the Permian shales is only 29–40% of the Lower Paleozoic shales, indicating that the methane adsorption capacities of the marine–terrestrial transitional shales are significantly lower than those of marine shales.

The density of adsorbed methane in the Permian shales ranges from 0.243 g/cm^3 to 0.360 g/cm^3 (Table 2), which is less than the density of liquid methane at its boiling point (e.g., 0.424 g/cm^3). There is a strong linear positive correlation between the adsorbed phase density and the TOC content (Figure 5a; Table 3), which indicates that samples with higher TOC content require higher pressures for excess adsorption to approach zero. Compared with the Longmaxi shales, there is no significant difference in the adsorbed phase density of samples with low TOC content (e.g., TOC < 4%) [8]. Due to the lack of Longmaxi shale samples with high TOC content, it is difficult to compare them directly. However, according to their trend line, it can be concluded that the adsorbed phase density of the Permian shales will be lower than that of the Longmaxi shales when TOC > 4%. In

contrast, the adsorbed phase density of the Niutitang shales is significantly higher than that of the Permian shales [14]. The values of pore structure parameter D range from 0.0091 mol^2/KJ^2 to 0.0132 mol^2/KJ^2, which are negatively related to the TOC content with a natural logarithm relation (Figure 5b) because organic matter in shale can provide more small pores than other minerals [17,31,32,59]. This regular pattern is also presented in the Longmaxi shales [8] (Figure 5b). However, due to the lack of samples with lower TOC content and the deviation of individual samples, the negative logarithm correlation is not obvious in the Niutitang shales [14] (Figure 5b). From the vertical perspective, the values of parameter D of the Permian shales are significantly larger than those of the marine shales [8,14], which indicates that the pore structure of marine–terrestrial transitional shales should be different from marine shales.

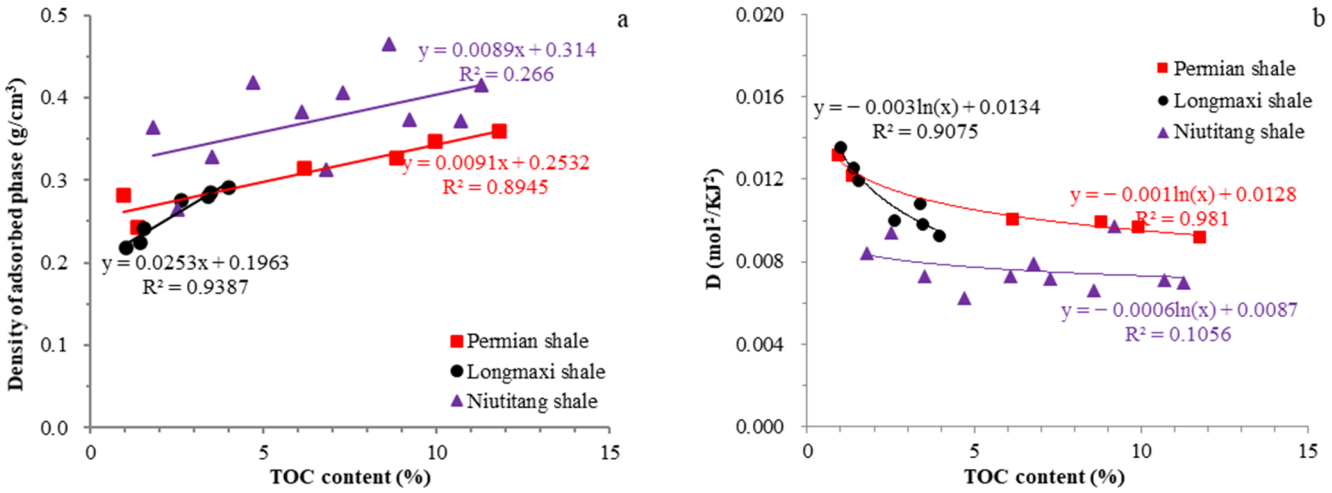

Figure 5. Plots showing the relationships between the density of the adsorbed phase with the TOC content (**a**) and the pore structure parameter D with the TOC content (**b**). (The Longmaxi and Niutitang shales are from Pan et al. [8] and Li et al. [14], respectively).

Gas adsorption is closely related to the pore structure of the adsorbent. The volume filling is mainly forming of methane adsorption in micropores (pore size < 2 nm); thus, the adsorbed amount depends on the volume of micropores. Monolayer–multilayer adsorption occurs on the surface of mesopores (2–50 nm) and macropores (>50 nm), and the adsorbed amount is related to the specific surface area [60]. Furthermore, the relationships between adsorption parameters and pore structure parameters of those shales are compared. The maximum excess and absolute adsorbed amounts of Permian shales have a strong linear positive correlation with the BET surface area and micropore volume (Figure 6; Table 3). The correlation with micropore volume is stronger than the correlation with surface area, because the adsorption capacities of micropores are stronger than larger pores [17,61]. Therefore, micropores in shales are the most important carriers for providing sites for methane adsorption, and the surface adsorption of mesopores and macropores is auxiliary [32,61,62]. The Permian shales show relatively smaller adsorption than the Longmaxi and Niutitang shales with the same micropore volume and BET surface area, indicating that the pore structure of shales with type III kerogen have lower methane adsorption capacities than marine shales with type I and/or type II kerogen.

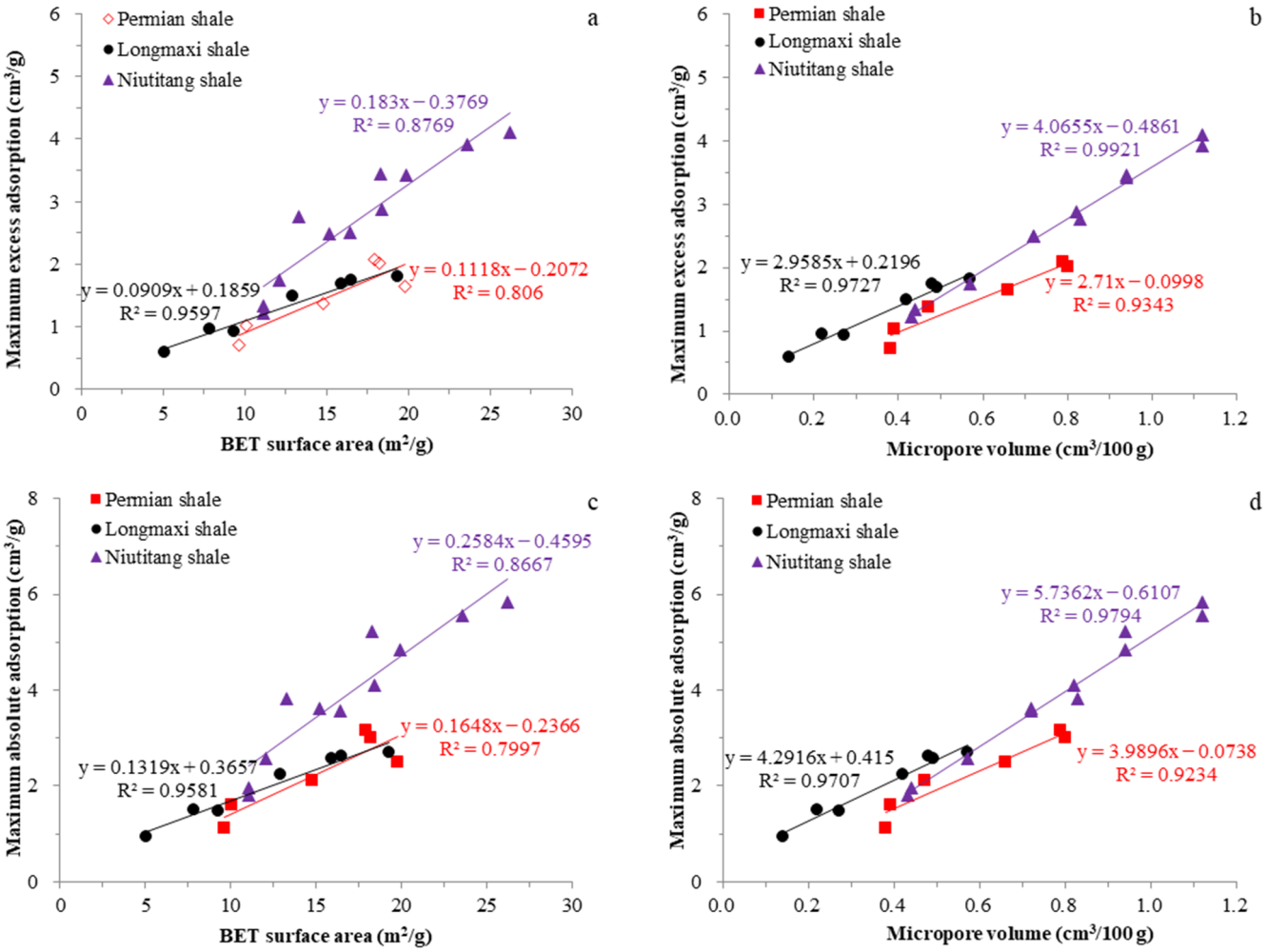

Figure 6. Plots showing the relationships between the maximum adsorption with the BET surface area (**a**,**c**) and the micropore volume (**b**,**d**) for the studied samples. (The Longmaxi and Niutitang shales are from Pan et al. [8] and Li et al. [14], respectively).

The above conclusion was also confirmed by FE-SEM images. At lower magnification, the organic matters are filled between the minerals. The black part is organic matter, and the gray part is minerals in the secondary electron (SE) images (Figure 7a). The intra-particle pores in organic matter have cylindrical, spherical, ellipsoid, and irregular shapes, which have sizes less than 200 nm (Figure 7b). The mesopores and macropores can be observed directly by FE-SEM. The interior of larger organic pores is composed of many smaller mesopores and micropores, which can greatly increase the internal specific surface area of shale (Figure 7c). The intra-particle and inter-particle pores of minerals are relatively rare. Moreover, the inter-particle pores of minerals are mainly mesopores and macropores (Figure 7d–f), which can provide a large amount of storage space for free gas [8,32]. A large number of pyrites are developed in the Permian shale, mainly in framboids and agglomerates (Figure 7d,e). Due to the supporting structure of pyrite, the pores of organic matter infilled in pyrite framboids are very developed (Figure 7f). Compared with the Lower Paleozoic shales in southern China [15], the connectivity of organic pores in Permian shale is poorer and most of them are distributed independently (Figure 7c). Both the Permian shale and marine shales are in the overmaturity stage. The type of kerogen should be an important factor for this difference. Therefore, further studies on type III kerogen shale are needed. Type I and type II kerogens contain more retained oil (or bitumen) than type III kerogen, and more gaseous hydrocarbons and more organic nanopores are formed during the process of thermal evolution [22].

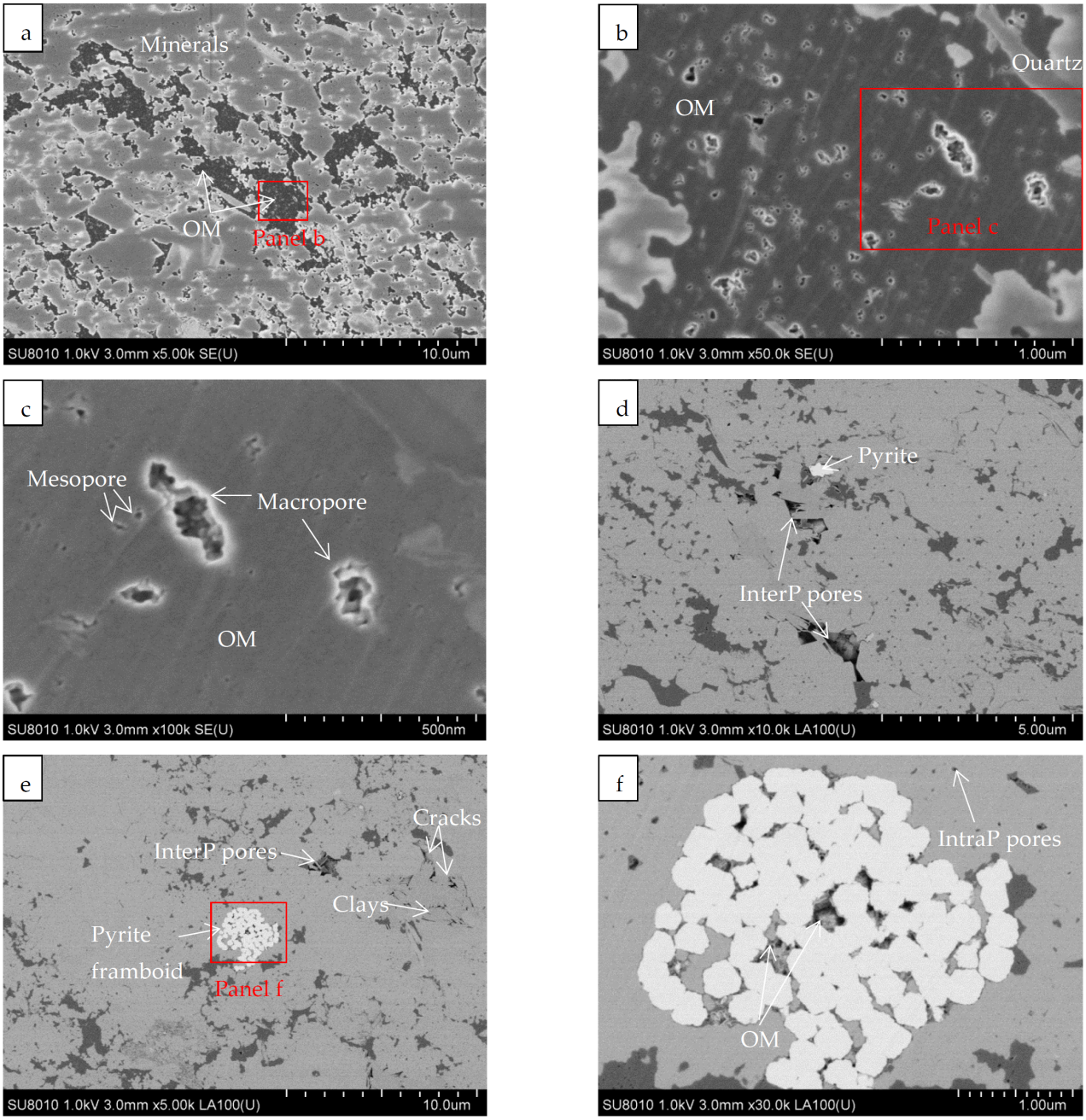

Figure 7. (**a**–**f**), FE-SEM images of the organic-rich Permian shale (Sample C1-7, TOC = 11.8%) with type III kerogen from the Lower Yangtze area. OM = organic matter; InterP pores = inter-particle pores; IntraP pores = intra-particle pores. ((**a**,**d**,**e**), Minerals; (**a**–**c**), OM pores; (**d**–**f**), Pyrite; (**d**,**e**), InterP pores; (**f**), IntraP pores).

In addition, it should be noted that there is a slight difference between the saturated adsorption phase volume calculated at 60 °C and the CO_2 micropore volume tested at 0 °C (Figure 8). For the samples with lower organic matter content (TOC < 6%), they are almost the same, while the micropore volume of samples with higher TOC content is slightly higher than the saturated adsorption phase volume. Similar phenomena were found in marine shales reported by Gai et al. [3]. Therefore, the CO_2 micropore volume can be used as a substitute index of methane adsorbed volume in dry shales without high-pressure adsorption experiment. Due to the limitation of the data, more adsorption experiments are needed to support this inference.

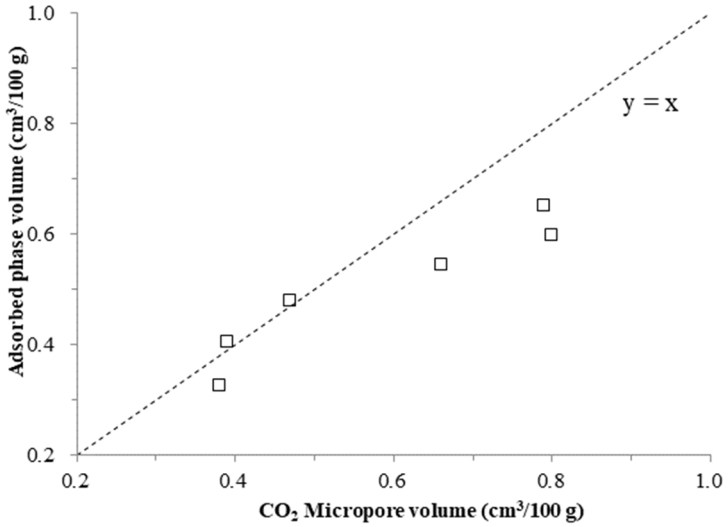

Figure 8. Plot showing the relationship between the adsorbed phase volume calculated at 60 °C and the CO_2 micropore volume tested at 0 °C for the studied samples.

4.3. Influence of Temperature on Adsorption Characteristics

The adsorption parameters of selected samples (C1-4, C1-7 and C1-10) under different temperatures are listed in Table 4, which are fitted by the SDR model. With increasing adsorption temperature, there is a strong linear positive correlation between the maximum absolute adsorption and the reciprocal of the Kelvin temperature (Figure 9a). Obviously, the density of the adsorbed phase is also positively correlated with the reciprocal of the Kelvin temperature (Figure 9b). The adsorbed phase volumes of organic-rich shales have a linear positive correlation with the reciprocal of the Kelvin temperature, and the CO_2 micropore volume basically falls on the extension line of this relationship (Figure 10). This can provide insight into why the adsorbed phase volume (measured at 60 °C) of shale samples with high TOC content is slightly lower than its CO_2 micropore volume (measured at 0 °C) (Figures 8 and 10). However, parameter D is not obviously affected by increasing temperature (Table 4), which shows that the variation in adsorption temperature has not caused obvious changes of pore structure in shale.

Table 4. The adsorption parameters of three selected samples (C1-4, C1-7 and C1-10).

Samples	Temperature	1/Temperature	n_{ex}^{max}	Pressure	D	ρ_{ad}	n_{ab}^{max}	V_{ad}
	(°C)	(1/K)	(cm^3/g) [1]	(MPa)	(mol^2/KJ^2)	(g/cm^3)	(cm^3/g) [1]	($cm^3/100$ g)
C1-4	40	0.003195	0.80	~8	0.0126	0.26	1.23	0.34
	60	0.003003	0.72	~8		0.24	1.11	0.33
	80	0.002833	0.61	~9		0.23	0.98	0.31
	150	0.002364	0.37	~10		0.16	0.65	0.29
C1-7	40	0.003195	2.25	~9	0.0091	0.37	3.30	0.64
	60	0.003003	2.02	~9		0.36	3.01	0.6
	80	0.002833	1.84	~11		0.33	2.83	0.61
	100	0.002681	1.57	~12		0.30	2.43	0.57
	150	0.002364	1.27	~14		0.26	1.99	0.55
C1-10	40	0.003195	1.84	~9	0.0099	0.33	2.71	0.58
	60	0.003003	1.64	~10		0.33	2.49	0.54
	80	0.002833	1.48	~11		0.30	2.26	0.53
	100	0.002681	1.21	~12		0.27	1.90	0.50
	120	0.002545	1.08	~13		0.25	1.75	0.50
	150	0.002364	0.86	~13		0.22	1.39	0.45

[1] 1 mmol/g = 16 mg/g = 22.4 cm^3/g rock @STP.

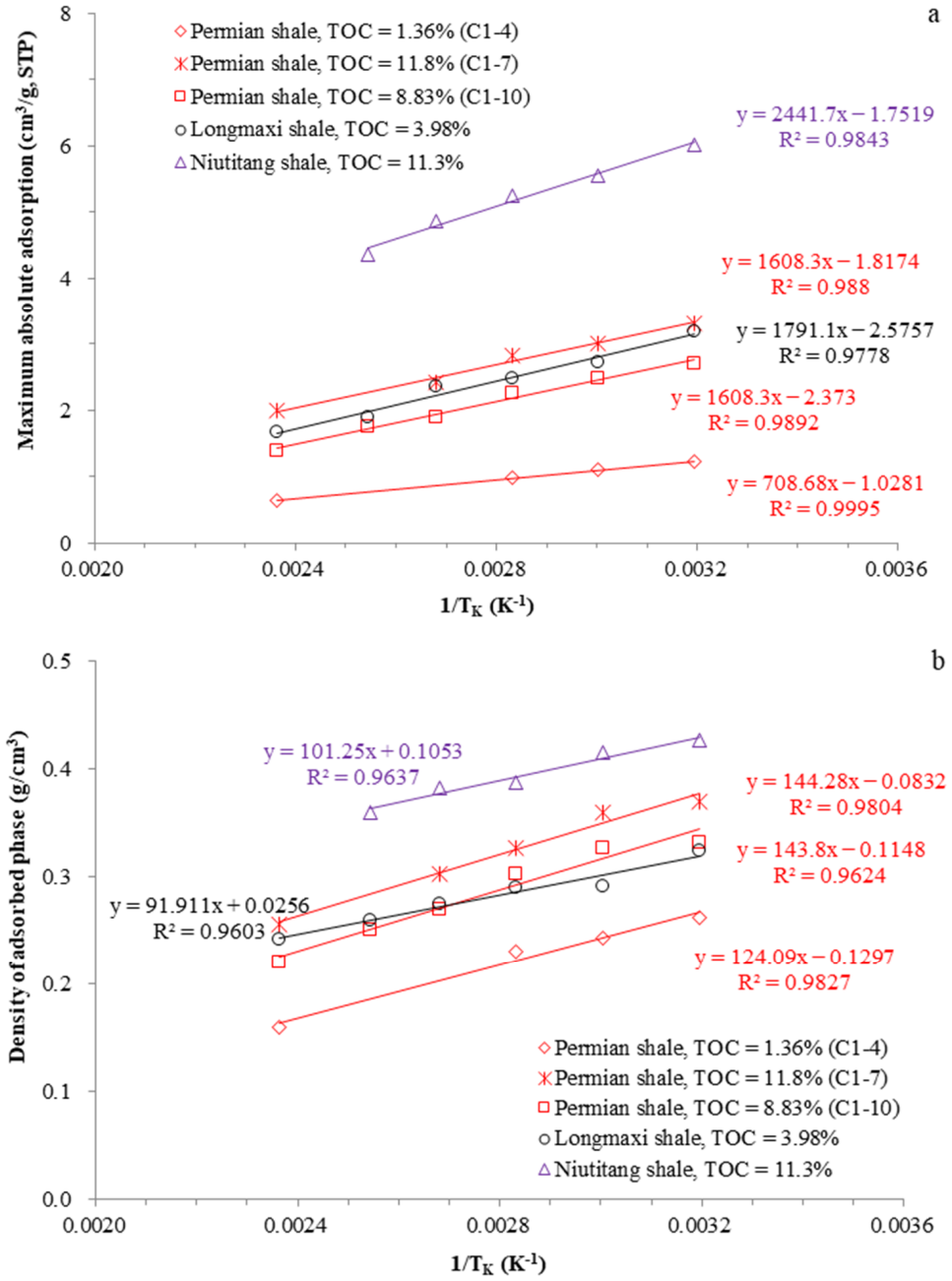

Figure 9. Plots showing the relationships between the reciprocal of the Kelvin temperature with the maximum absolute adsorption capacity (**a**) and the density of adsorbed phase (**b**) for shales. (The Longmaxi and Niutitang shales are from Pan et al. [8] and Li et al. [14], respectively).

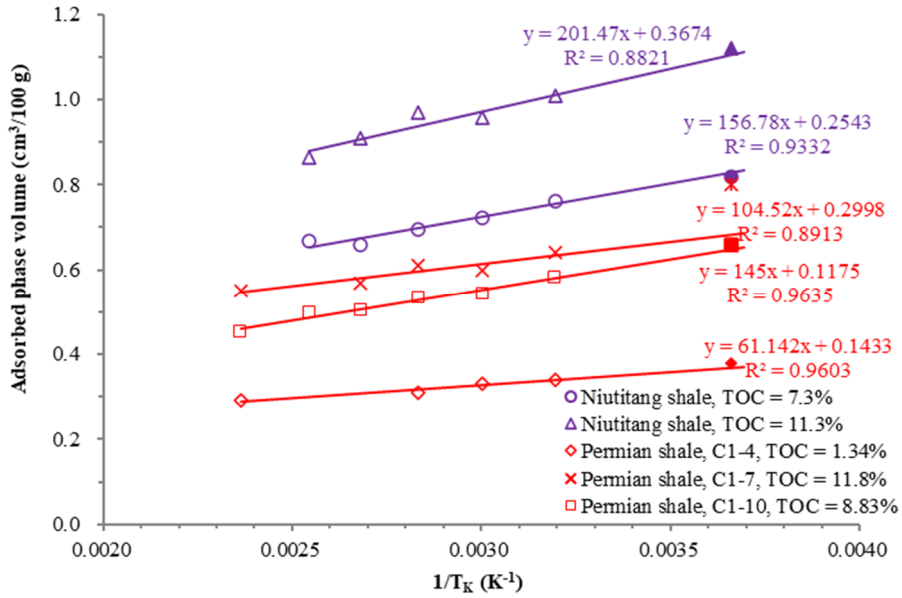

Figure 10. Plots showing the relationships between the reciprocal of the Kelvin temperature and the adsorbed phase volume of Permian and organic-rich Niutitang shales [14]. (The hollow icons represent the adsorbed phase volume, and the solid icons represent the CO_2 micropore volume obtained at 273.15 K).

The adsorption parameters of marine shale samples at different temperatures are also shown in Figures 9 and 10. Although their TOC contents are somewhat different, some analysis results can be drawn. The adsorption parameters of the Lower Cambrian shale sample (TOC = 11.3%) [14] are obviously larger than those of the Permian shale sample (C1-7, TOC = 11.8%), though the TOC content of the Lower Cambrian shale is slightly lower than that of the Permian sample. In particular, the maximum absolute adsorption amounts of the Niutitang shale sample are about 1.8–2.0 times those of the Permian sample, while the adsorbed phase densities are approximately 1.15–1.27 times and the adsorbed phase volumes are about 1.57–1.60 times, respectively (Figure 9). Although the TOC content of the Lower Silurian shale sample (TOC = 3.98%) [8] is less than half of the Permian shale sample (C1-10, TOC = 8.83%), its absolute adsorption amounts are larger than those of the Permian shale sample. The adsorbed phase volumes of Permian shale samples at different experimental temperatures are significantly smaller than those of the Niutitang shale samples with similar TOC content (Figure 10). However, the number of samples is limited. Therefore, the phenomena observed in those samples may not be applicable to all shale samples.

4.4. Adsorption Thermodynamics

As shown in Figure 11a, the absolute adsorption amounts of Sample C1-7 and C1-10 are set as 1.5 cm^3/g rock and 2.0 cm^3/g rock, and the correlation coefficients are as high as 0.99 (Figure 11a). The isosteric heats and standard entropies are derived from the slopes and intercepts of the regressed lines, which are slightly reduced with the decrease in absolute adsorption. According to the studies reported by Tian et al. [7] on the Lower Silurian shales in the southeastern margin of the Sichuan Basin and Li et al. [14] on the Lower Cambrian shales in northern Guizhou, the thermodynamic parameters of marine shales fall between type I and type II kerogens [53] (Figure 11b). The isosteric heats and standard entropies of shales are affected by both organic matter type and thermal maturity [53,63], which have no obvious correlation with organic matter content [14]. With the transition of organic matter from type I to type III kerogen, the isosteric heats increase, while the standard entropies decrease. The Permian shales in the Lower Yangtze area is obviously different from the

marine shales, and the values exceed type II kerogen and are close to type III kerogen (Figure 11b).

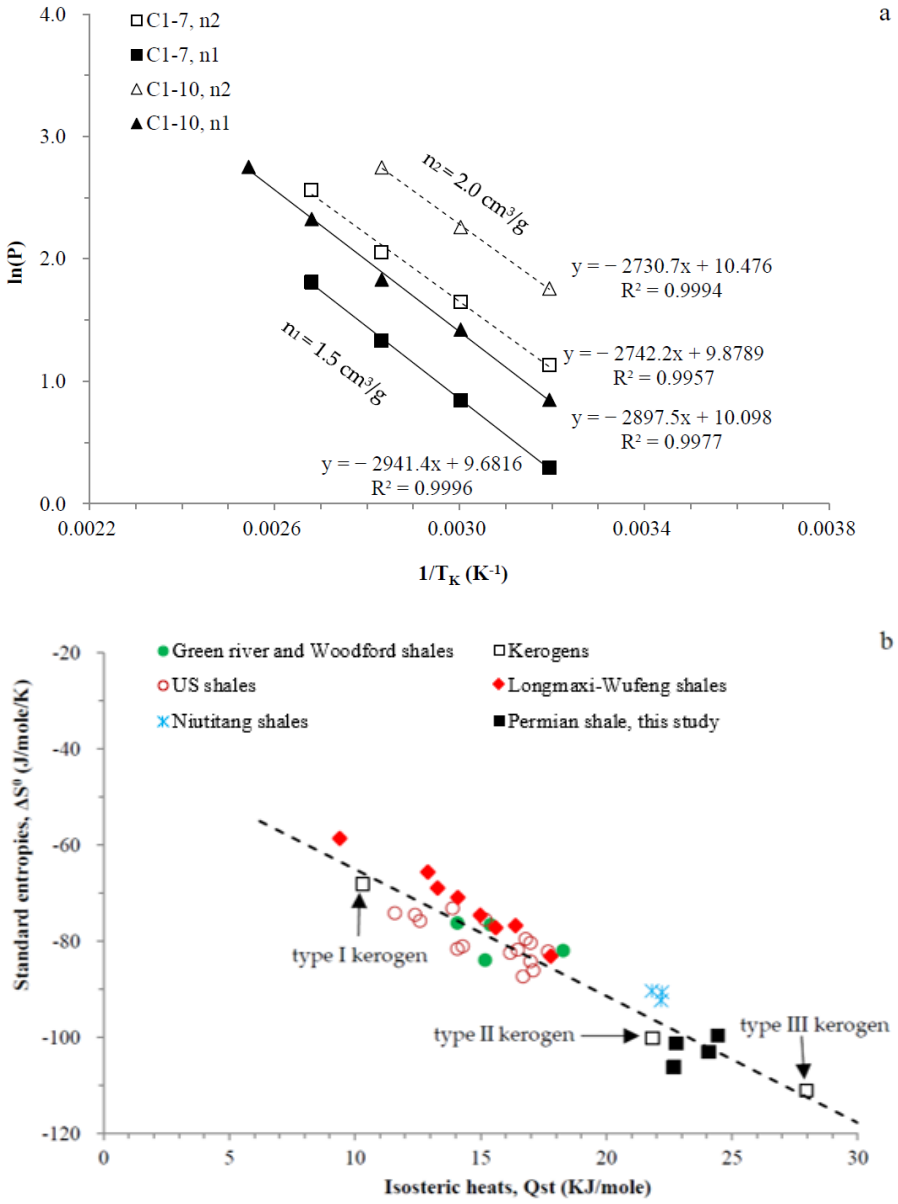

Figure 11. (**a**) Plots of ln(P) versus the reciprocal of the Kelvin temperature of Sample C1-7 and C1-10; (**b**) The linear relationship between the isosteric heats and standard entropies for the Permian shale and other shales and kerogens [7,14,53,63].

4.5. Methane Storage Capacity of the Permian Shales

The current geothermal gradient in the Lower Yangtze area ranges between 19–25 °C/km [38]. Wang et al. [64] reported that the geothermal gradients of several wells near the Wuhu block were 20.9, 24.1, 23 and 21 °C/km, with an average of 22.3 °C/km. Therefore, the geothermal gradient is set at 22 °C/km with a surface temperature of 15 °C. The fluid pressure coefficient of shale reservoirs is greatly affected by the tectonic stress field. Overpressure exists in the structural stability area or fold compression area, with a pressure coefficient reaching 1.5, while hydrostatic pressure occurs mostly in the uplift and tension area, with a pressure coefficient of approximately 1.0 [65]. Due to the lack of detailed exploration data on the Permian shales in the study area, the water saturation was set as 30% in the hydrostatic pressure area and 20% in the overpressure area, which were based on the exploration data of the Longmaxi shales in the Upper Yangtze area [8,66,67].

The experimental temperature range is 40–150 °C, and the pressure range is 0–35 MPa. According to the set geological parameters, the corresponding burial depths are about 1200–6000 m and 0–3500 m, respectively. Combined with the high-pressure adsorption and porosity, the MSC geological models of the Permian shale systems are established under two different pressure coefficients (1.0 and 1.5) (Figure 12). The free gas content is mainly affected by the fluid pressure coefficient, burial depth, TOC content, and porosity. However, the fluid pressure coefficient has a tiny influence on adsorption gas, especially when the buried depth is more than 3000 m. With the increase in the fluid pressure coefficient, the free gas content increases, thus increasing the MSC of shale. The free gas increases with increasing burial depth, while the adsorption gas decreases in the depth of 1200–6000 m. When the burial depth of the shale system is greater than 2000 m, the burial depth mainly affects the ratio of adsorbed gas to free gas, but the total gas content has no obvious change. For the shallow shale reservoir (depth < 2000 m), the burial depth has an important influence on the content and proportion of gas. Although the water saturation is considered, the interaction of water–shale–rock is ignored in this study. In fact, H_2O molecules are preferentially adsorbed on the hydrophilic group, which usually reduces the methane adsorption capacity of shale [68,69]. The MSC model of shale samples represent the maximum gas content of shale reservoirs. Therefore, The GIP of real shale reservoir should be less than the predictive MSC model.

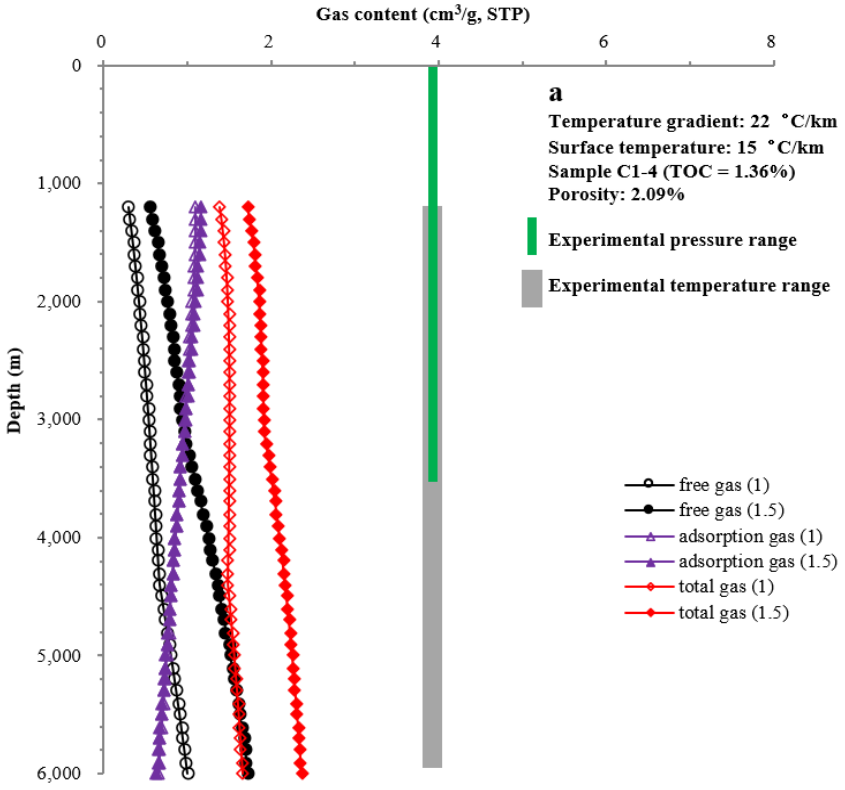

Figure 12. *Cont.*

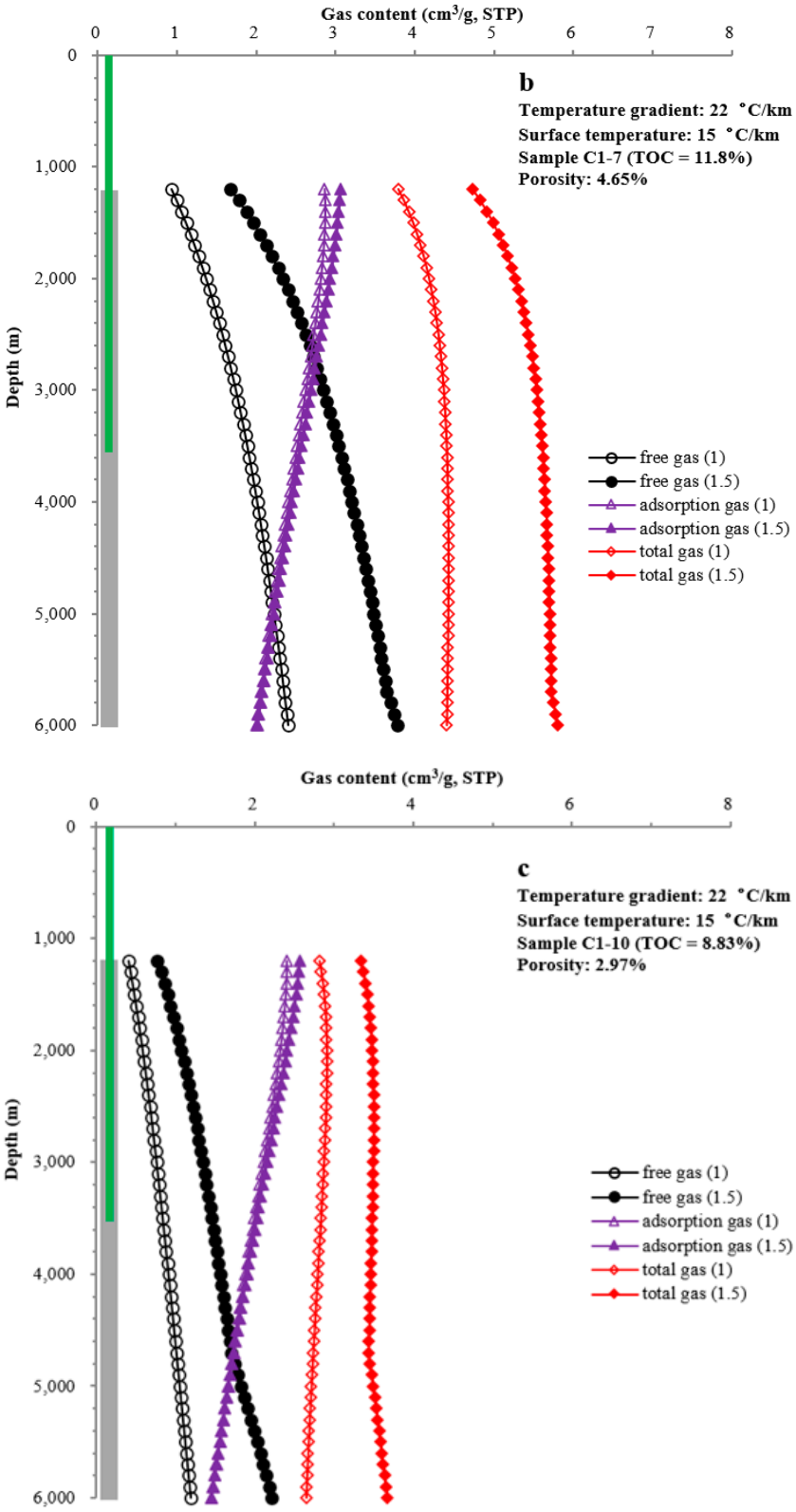

Figure 12. The MSC models of the Permian shale reservoirs based on difference TOC content samples ((**a**) Sample C1-4 with a TOC content of 1.36% and a total porosity of 2.09%. (**b**) Sample C1-7 with a TOC content of 11.8% and a total porosity of 4.65%. (**c**) Sample C1-10 with a TOC content of 8.83% and a total porosity of 2.97%). The numbers in legend mean the fluid pressure coefficient. The water saturation is 20% for reservoir with a pressure coefficient of 1.5 and 30% for reservoir with a pressure coefficient of 1.0. The geothermal gradient is 22 °C/km with a surface temperature of 15 °C.

Furthermore, the relationships between the MSC of Permian samples with the TOC content and porosity were constructed and compared with the Lower Silurian shale (Figures 13 and 14). The set reservoir temperature was 60 °C, corresponding to the burial depth of approximately 2000 m. According to Figure 13, the total gas content and adsorbed gas content of the Permian shales are positively correlated with the TOC content, while the free gas content is mainly controlled by the fluid pressure of shale reservoir system. At present, the Permian shale reservoirs in the Lower Yangtze area have a burial depth of less than 4000 m, and most of them are controlled by hydrostatic pressure. If we refer to the GIP index of economic shale gas reservoirs (e.g., 2.5 m^3/t) [13], the corresponding TOC contents are at least 5.6% and 3.6% under hydrostatic pressure and 1.5 times hydrostatic pressure, respectively. With the same pressure coefficient, water saturation, and geothermal gradient, the MSC of the Permian shales is significantly lower than that of the Longmaxi shales. For Permian shales, a higher TOC content is required to achieve the same MSC as Longmaxi shales.

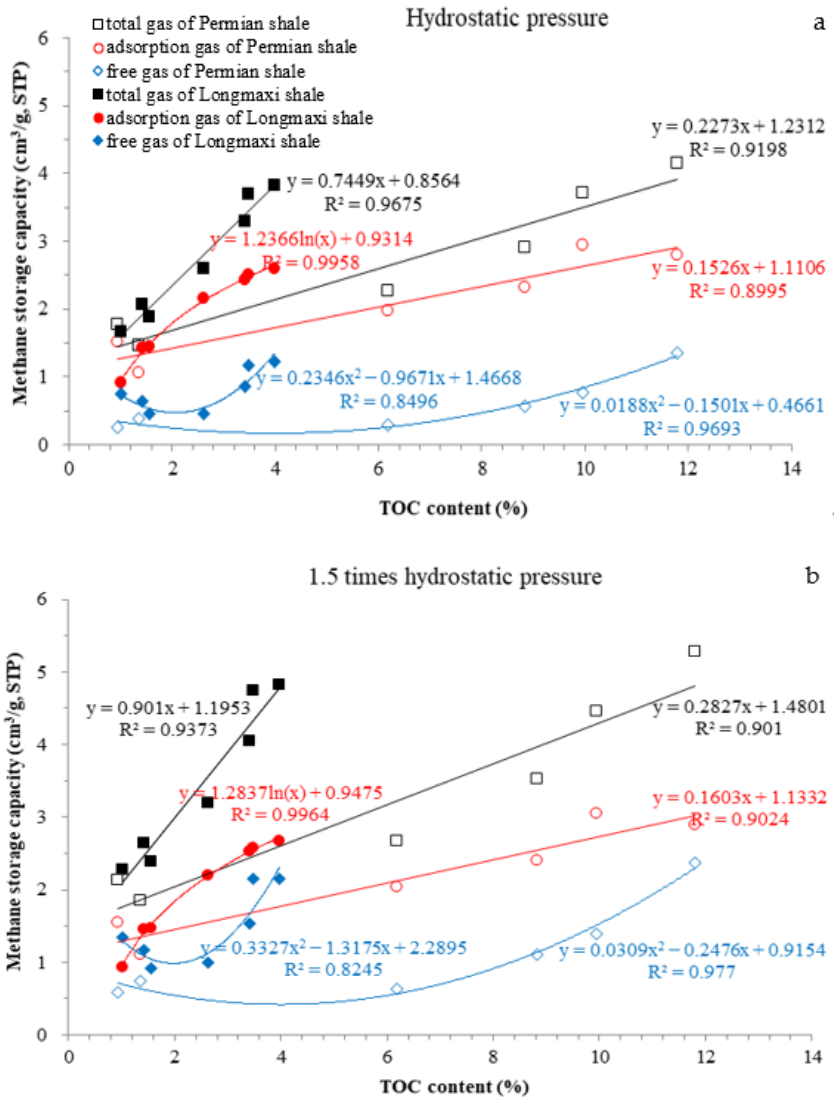

Figure 13. Plots showing the relationships of the TOC content and the MSC of the Permian and Lower Silurian shales [8] under hydrostatic pressure (**a**) and 1.5 times hydrostatic pressure (**b**). The set reservoir temperature is 60 °C, corresponding buried depth of approximately 2000 m. The water saturation is 30% for the reservoir with hydrostatic pressure, and 20% for the reservoir with 1.5 times hydrostatic pressure. (All drawings have the same icons shown in the first).

According to Figure 14, the porosity of Permian shales needs to reach 3.35% to match the MSC of 2.5 m^3/t at hydrostatic pressure. It is mainly composed of adsorption gas, accounting for 73% (Figure 14a). The increase in the pressure coefficient can obviously increase the free gas content. The porosity corresponding to a MSC of 2.5 m^3/t at 1.5 times hydrostatic pressure is 2.78%, and the proportion of adsorption gas is 58% (Figure 14b). Compared with the Longmaxi shales, they have similar free gas contents under the same porosity, but the adsorbed gas contents of the Permian shales are lower than the Longmaxi shales. It should be noted that the porosity of the Permian shales is also controlled by the TOC content [17]. Therefore, the TOC content is the most important parameter for evaluating Permian shales, which is the same as marine shales [7,32,63].

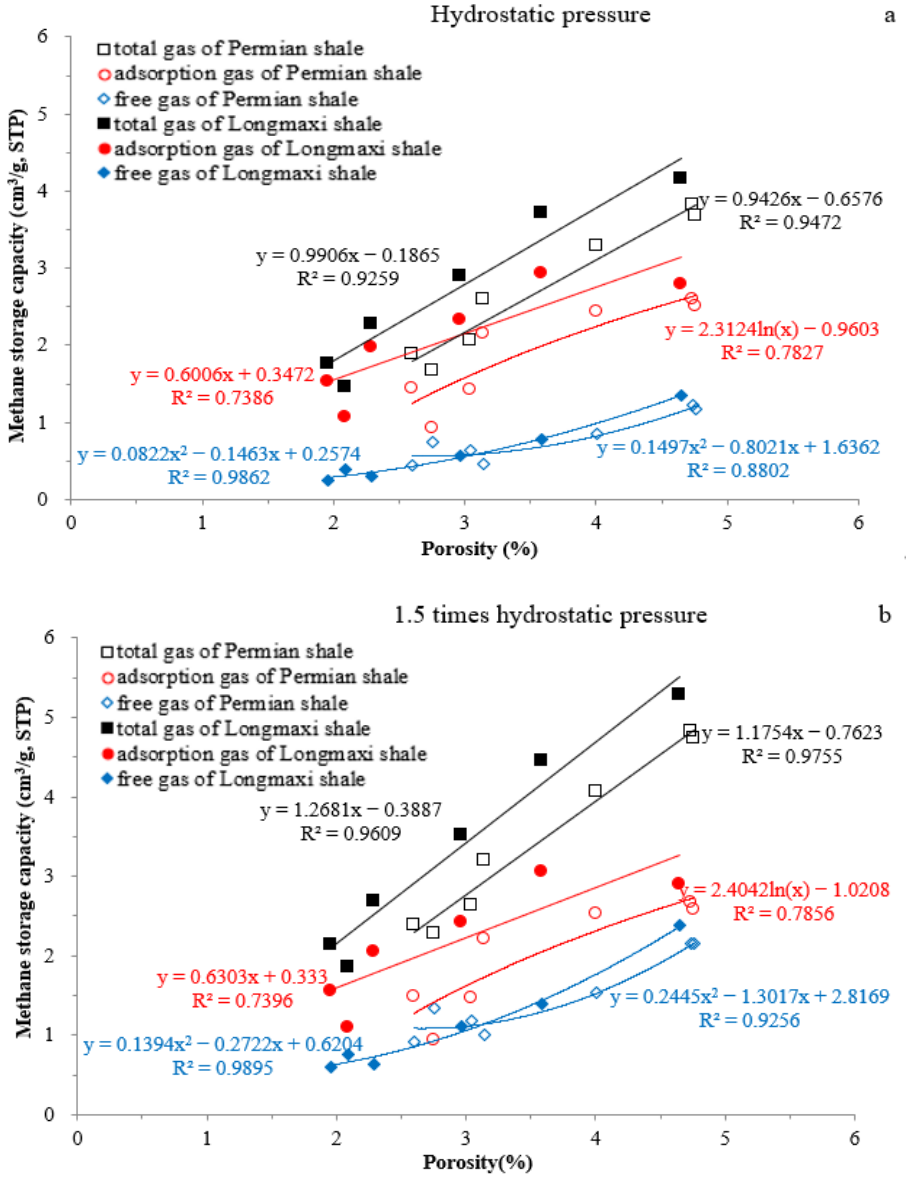

Figure 14. Plots showing the relationships of the porosity and the MSC of the Permian and Lower Silurian shales [8] under hydrostatic pressure (**a**) and 1.5 times hydrostatic pressure (**b**). The set reservoir temperature is 60 °C, corresponding buried depth of approximately 2000 m. The water saturation is 30% for the reservoir with hydrostatic pressure, and 20% for the reservoir with 1.5 times hydrostatic pressure.

4.6. Geological Significance

The organic matter type of the Permian shales is type III kerogen, which may be the fundamental reason for the unsatisfactory exploration of Permian shales in southern China. Due to the undeveloped nanopores in organic matter, the porosity of the Permian shales is relatively low. The MSC of the Permian shales is lower than the marine shales with the same TOC content. Therefore, the Permian shales needs a higher TOC content or a higher porosity to achieve the same GIP as the marine shales. Furthermore, the higher the temperature is, the lower the adsorbed phase density and the maximum adsorption, and the lower the density of free methane [70]. With an increasing pressure coefficient, the free gas increases, but the adsorption gas is hardly affected when the burial depth is more than 2000 m. Overpressure is more favorable for shale gas preservation. Furthermore, the relatively low geothermal gradient is more beneficial for gas accumulation and preservation. Therefore, the burial depth is a key controlling factor of the GIP of shale reservoirs.

Li et al. [71] reported that the lower limit of TOC content for the Longmaxi shales in the southern Sichuan Basin should be 1.0%, while the lower limit of porosity should be 1.2%. Zhao et al. [13] considered that the enrichment conditions of economic marine shale in South China should include TOC > 2%, porosity > 3%, and gas content > 2.5 m^3/t. In addition, the type of organic matter is also a very important factor in determining the lower limit index of shale. Therefore, we consider that the evaluation index system of marine shales may not be suitable for the marine–terrestrial transitional Permian shales. The Permian shales should have higher TOC content (e.g., >5%) and higher porosity (e.g., >3%) for blocks with preferential development potential. In addition, the Permian shale blocks with larger burial depths (>2000 m) and fluid overpressure conditions are the most promising breakthroughs in the Lower Yangtze area.

5. Conclusions

Based on the high-pressure adsorption characteristics and methane storage capacities of the Permian shales with type III kerogen in the Lower Yangtze area, the following conclusions have been drawn:

(1) The maximum adsorption and adsorbed phase density of the Permian shales are mainly constrained by TOC content and temperature, which are positively related to TOC but adversely related to temperature. The micropores are the most important carriers for providing sites for methane adsorption.
(2) The methane adsorption capacity of Permian shales is significantly lower than that of the marine shales, which is mainly due to undeveloped organic pores. The type of organic matter is also another key factor affecting the MSC of shale.
(3) The evaluation index of marine shales may not be suitable for the marine–terrestrial transitional shales. The Permian shales with development potential in the Lower Yangtze area should have a higher TOC content (e.g., >5%) and porosity (e.g., >3%). The overpressure stable reservoirs with rich-organic shale and deep burial depth are preferred to be selected for the next exploration.

Author Contributions: Conceptualization, L.P. and L.C.; methodology, L.P.; software, L.P.; validation, L.P., P.C. and H.G.; formal analysis, L.P.; investigation, P.C.; resources, L.P. and P.C.; data curation, H.G.; writing—original draft preparation, L.P.; writing—review and editing, L.C.; visualization, L.P.; supervision, L.C.; project administration, L.P.; funding acquisition, L.P. and L.C. All authors have read and agreed to the published version of the manuscript.

Funding: This research was funded by the Natural Science Foundation of Guangxi Province (grant number AD19245151, AD19245111 and 2018GXNSFBA138057), the Start-up Foundation of Beibu Gulf University (grant number 2018KYQD20 and 2016PY-GJ06), and the Natural Science Foundation of Guangdong Province (grant number 2021A1515011381).

Institutional Review Board Statement: Not applicable.

Informed Consent Statement: Not applicable.

Data Availability Statement: Not applicable.

Acknowledgments: The authors gratefully acknowledge the Natural Science Foundation of Guangxi Province and the Natural Science Foundation of Guangdong Province. We are indebted to Xianming Xiao and Hui Tian for their insightful suggestions on the original manuscript. All anonymous reviewers are gratefully acknowledged.

Conflicts of Interest: The authors declare no conflict of interest.

References

1. Pang, F.; Zhang, Z.; Zhang, J.; Chen, K.; Shi, D.; Bao, S.; Li, S.; Guo, T. Progress and prospect on exploration and development of shale gas in the Yangtze River Economic Belt. *Earth Sci.* **2020**, *45*, 2152–2159.
2. Zou, X.; Li, X.; Zhang, L.; Li, H.; Guo, M.; Zhao, P. Characteristics of Pore Structure and Gas Content of the Lower Paleozoic Shale from the Upper Yangtze Plate, South China. *Energies* **2021**, *14*, 7603. [CrossRef]
3. Gai, H.; Li, T.; Wang, X.; Tian, H.; Xiao, X.; Zhou, Q. Methane adsorption characteristics of overmature Lower Cambrian shales of deepwater shelf facies in Southwest China. *Mar. Pet. Geol.* **2020**, *120*, 104565. [CrossRef]
4. Zou, C.; Zhu, R.; Chen, Z.; Ogg, J.; Wu, S.; Dong, D.; Qiu, Z.; Wang, Y.; Wang, L.; Lin, S. Organic-matter-rich shales of China. *Earth-Sci. Rev.* **2019**, *189*, 51–78. [CrossRef]
5. Zhang, J.; Li, X.; Zhang, X.; Zhang, M.; Cong, G.; Zhang, G.; Wang, F. Geochemical and geological characterization of marine–continental transitional shales from Longtan Formation in Yangtze area, South China. *Mar. Pet. Geol.* **2018**, *96*, 1–15. [CrossRef]
6. Zhang, T.; Zhang, Y.; Jia, M.; Shao, D.; Yan, J. Key scientific issues on controlling the variation of gas contents of Cambrian marine shales in Southern China. *Bull. Min. Petrol. Geol.* **2018**, *37*, 572–579.
7. Tian, H.; Li, T.; Zhang, T.; Xiao, X. Characterization of methane adsorption on overmature Lower Silurian-Upper Ordovician shales in Sichuan Basin, southwest China: Experimental results and geological implications. *Int. J. Coal Geol.* **2016**, *156*, 36–49. [CrossRef]
8. Pan, L.; Xiao, X.; Tian, H.; Zhou, Q.; Cheng, P. Geological models of gas in place of the Longmaxi shale in Southeast Chongqing, South China. *Mar. Pet. Geol.* **2016**, *73*, 433–444. [CrossRef]
9. Mahmud, H.B.; Ermila, M.; Bennour, Z.; Mahmud, W.M. A review of fracturing technologies utilized in shale gas resources. In *Shale Gas Production-Lessons Learned*; IntechOpen: London, UK, 2020; pp. 1–24. Available online: https://www.intechopen.com/online-first/72128 (accessed on 16 May 2020).
10. Wang, S.; Gao, W.; Guo, T.; Bao, S.; Jin, J.; Xu, Q. The discovery of shale gas, coalbed gas and tight sandstone gas in Permian Longtan Formation, northern Guizhou Province. *Geol. China* **2020**, *47*, 249–250.
11. Shi, G.; Li, J.; Liao, S.; Wu, T.; Huang, N.; Fang, C. Discovery of Permian shale gas in the well Wanyoudi No. 1, Xuancheng, Anhui Province. *Geol. China* **2020**, *48*, 669–670.
12. Chen, Z.; Wang, Z.; Li, S. Geological condition analysis of shale gas and coalbed methane of Leping Formation in Well Quye1 of Pingle Depression. *Pet. Geo. Rec. Eff.* **2019**, *26*, 50–55.
13. Zhao, W.; Li, J.; Yang, T.; Wang, S.; Huang, J. Geological difference and its significance of marine shale gases in South China. *Pet. Explor. Dev.* **2016**, *43*, 547–559. [CrossRef]
14. Li, T.; Tian, H.; Xiao, X.; Cheng, P.; Zhou, Q.; Wei, Q. Geochemical characterization and methane adsorption capacity of overmature organic-rich Lower Cambrian shales in northeast Guizhou region, southwest China. *Mar. Pet. Geol.* **2017**, *86*, 858–873. [CrossRef]
15. Tian, H.; Pan, L.; Zhang, T.; Xiao, X.; Meng, Z.; Huang, B. Pore characterization of organic-rich Lower Cambrian shales in Qiannan Depression of Guizhou Province, Southwestern China. *Mar. Pet. Geol.* **2015**, *62*, 28–43. [CrossRef]
16. Tian, H.; Pan, L.; Xiao, X.; Wilkins, R.W.T.; Meng, Z.; Huang, B. A preliminary study on the pore characterization of Lower Silurian black shales in the Chuandong Thrust Fold Belt, southwestern China using low pressure N_2 adsorption and FE-SEM methods. *Mar. Pet. Geol.* **2013**, *48*, 8–19. [CrossRef]
17. Pan, L.; Xiao, X.; Tian, H.; Zhou, Q.; Chen, J.; Li, T.; Wei, Q. A preliminary study on the characterization and controlling factors of porosity and pore structure of the Permian shales in Lower Yangtze region, Eastern China. *Int. J. Coal Geol.* **2015**, *146*, 68–78. [CrossRef]
18. Zhao, P.; Gao, B.; Guo, Z.; Wei, Z. Exploration potential of marine-continental transitional and deep-water shelf shale gas in Upper Permian, Sichuan Basin. *Petrol. Geol. Exp.* **2020**, *42*, 335–344.
19. Gai, H.; Tian, H.; Xiao, X. Late gas generation potential for different types of shale source rocks: Implications from pyrolysis experiments. *Int. J. Coal Geol.* **2018**, *193*, 16–29. [CrossRef]
20. Mahlstedt, N.; Horsfield, B. Metagenetic methane generation in gas shales I. Screening protocols using immature samples. *Mar. Pet. Geol.* **2012**, *31*, 27–42. [CrossRef]
21. Dai, H.; Shen, B.; Li, K.; Zhang, X.; Xu, X.; Xu, Z.; Zhou, J. Characteristics and hydrocarbon-generating process of the organic-rich shale of Permian Dalong Formation in North Sichuan: Pyrolysis experiments with geological constrain. *J. Nanjing Univ. (Nat. Sci.)* **2020**, *56*, 382–392.
22. Chen, J.; Xiao, X. Evolution of nanoporosity in organic-rich shales during thermal maturation. *Fuel* **2014**, *129*, 173–181. [CrossRef]

23. Liang, D.; Guo, T.; Chen, J.; Bian, L.; Zhao, Z. Some progresses on studies of hydrocarbon generation and accumulation in marine sedimentary regions, Southern China (Part 1): Distribution of four suits of regional marine source rocks. *Mar. Orig. Pet. Geol.* **2008**, *13*, 1–16.
24. Li, Q.; Xu, S.; Chen, K.; Song, T.; Meng, F.; He, S.; Lu, Y.; Shi, W.; Gou, Q.; Wang, Y. Analysis of shale gas accumulation conditions of Upper Permian in the Lower Yangtze Region. *Geol. China* **2020**. Available online: https://kns.cnki.net/kcms/dtail/11.1167.-p.20200429.1018.004.html (accessed on 16 April 2020).
25. Huang, B.; Hao, H.; Jin, Q.; Zhou, G.; Zhao, X. Characterization of pores and methane sorption capacity of Permian shales in Southeast Anhui, Lower Yangtze region. *Nat. Gas Geosci.* **2015**, *26*, 1516–1524.
26. Chen, P.; Zhang, M.; Xu, Y.; Liu, J.; Du, X.; Hu, X.; Lu, Y. The shale reservoir characteristic of Dalong Formation Upper Permian in Chaohu-Jingxian, Lower Yangtze area. *Acta Pet. Sin.* **2013**, *29*, 2925–2935.
27. Ambrose, R.J.; Hartman, R.C.; Diaz-Campos, M.; Akkutlu, I.Y.; Songdergeld, C.H. Shale gas-in-place calculations part I: New pore-scale considerations. *SPE J.* **2012**, *17*, 219–229. [CrossRef]
28. Curtis, J.B. Fractured shale-gas systems. *AAPG Bull.* **2002**, *86*, 1921–1938.
29. Zhang, B.; Shan, B.; Zhao, Y.; Zhang, L. Review of formation and gas characteristics in shale gas reservoirs. *Energies* **2020**, *13*, 5427. [CrossRef]
30. Rexer, T.F.; Mathia, E.J.; Aplin, A.C.; Thomas, K.M. High-pressure methane adsorption and characterization of pores in Posidonia shales and isolated kerogens. *Energy Fuels* **2014**, *28*, 2886–2901. [CrossRef]
31. Rexer, T.F.T.; Benham, M.J.; Aplin, A.C.; Thomas, K.M. Methane adsorption on shale under simulated geological temperature and pressure conditions. *Energy Fuels* **2013**, *27*, 3099–3106. [CrossRef]
32. Ross, D.J.K.; Bustin, R.M. The importance of shale composition and pore structure upon gas storage potential of shale gas reservoirs. *Mar. Pet. Geol.* **2009**, *26*, 916–927. [CrossRef]
33. Gong, L.; Zhang, Y.; Li, N.; Gu, Z.; Ding, B.; Zhu, C. Molecular Investigation on the Displacement Characteristics of CH_4 by CO_2, N_2 and Their Mixture in a Composite Shale Model. *Energies* **2021**, *14*, 2. [CrossRef]
34. Song, R.; Wang, Y.; Sun, S.; Liu, J. Characterization and microfabrication of natural porous rocks: From micro-CT imaging and digital rock modelling to micro-3D-printed rock analogs. *J. Pet. Sci. Eng.* **2021**, *205*, 108827. [CrossRef]
35. Middleton, R.; Viswanathan, H.; Currier, R.; Gupta, R. CO_2 as a fracturing fluid: Potential for commercial-scale shale gas production and CO_2 sequestration. *Energy Procedia* **2014**, *63*, 7780–7784. [CrossRef]
36. Feng, Z.; He, Y.; Wu, S. Listhofacies paleogeography of Permian Middle and Lower Yangtze region. *Acta Sedimentol. Sin.* **1993**, *11*, 13–24.
37. Zhu, G.; Xu, J.; Liu, G.; Li, S.; Yu, P. Tectonic pattern and dynamic mechanism of the foreland deformation in the Lower Yangtze region. *Reg. Geol. China* **1999**, *18*, 73–79.
38. Yuan, Y.; Guo, T.; Fu, X.; Lu, Q.; Hu, S. Thermal history and secondary hydrocarbon generation intensity of marine source rocks in Lower Yangtze Area. *Geoscience* **2006**, *20*, 283–290.
39. Zhang, H.; Zhou, L.; Li, J. Hydrocarbon exploration potential analysis of the Lower Marine Formation assemblage in the Lower Yangtze Region. *Pet. Geol. Exp.* **2006**, *28*, 15–20.
40. Yu, K.; Guo, N. Evaluation on the geology conditions of the Lower Paleozoic hydrocarbon in Lower Yangtze area. *Pet. Geol. Exp.* **2001**, *23*, 41–46.
41. Loucks, R.G.; Reed, R.M.; Ruppel, S.C.; Jarcie, D.M. Morphology, genesis, and distribution of nanometer-scale pores in siliceous mudstones of the Mississippian Barnett Shale. *J. Sediment. Res.* **2009**, *79*, 848–861. [CrossRef]
42. Gasparik, M.; Rexer, T.F.T.; Aplin, A.C.; Billemont, P.; Weireld, G.D.; Gensterblum, Y.; Henry, M.; Krooss, B.M.; Liu, S.B.; Ma, X.Z.; et al. First international inter-laboratory comparison of high-pressure CH_4, CO_2 and C_2H_6 sorption isotherms on carbonaceous shales. *Int. J. Coal Geol.* **2014**, *132*, 131–146. [CrossRef]
43. Ottiger, S.; Pini, R.; Storti, G.; Mazzotti, M. Competitive adsorption equilibria of CO_2 and CH_4 on a dry coal. *Adsorption* **2008**, *14*, 539–556. [CrossRef]
44. Pini, R.; Ottiger, S.; Burlini, L.; Storti, G.; Mazzotti, M. Sorption of carbon dioxide, methane and nitrogen in dry coals at high pressure and moderate temperature. *Int. J. Greenh. Gas Control* **2010**, *4*, 90–101. [CrossRef]
45. Bae, J.S.; Bhatia, S.K. High-pressure adsorption of methane and carbon dioxide on coal. *Energy Fuels* **2006**, *20*, 2599–2607. [CrossRef]
46. Murata, K.; El-Merraoui, M.; Kaneko, K. A new determination method of absolute adsorption isotherm of supercritical gases under high pressure with a special relevance to density-functional theory study. *J. Chem. Phys.* **2001**, *114*, 4196–4205. [CrossRef]
47. Langmuir, I. The adsorption of gases on plane surfaces of glass, mica and platinum. *J. Am. Chem. Soc.* **1918**, *40*, 1361–1403. [CrossRef]
48. Sakurovs, R.; Day, S.; Weir, S.; Duffy, G. Application of a modified Dubinin- Radushkevich equation to adsorption of gases by coals under supercritical conditions. *Energy Fuels* **2007**, *21*, 992–997. [CrossRef]
49. Gensterblum, Y.; Merkel, A.; Busch, A.; Krooss, B.M. High-pressure CH_4 and CO_2 sorption isotherms as a function of coal maturity and the influence of moisture. *Int. J. Coal Geol.* **2013**, *118*, 45–57. [CrossRef]
50. Gensterblum, Y.; Merkel, A.; Busch, A.; Krooss, B.M.; Littke, R. Gas saturation and CO_2 enhancement potential of coalbed methane reservoirs as a function of depth. *AAPG Bull.* **2014**, *98*, 395–420. [CrossRef]

51. White, C.M.; Smith, D.H.; Jones, K.L.; Goodman, A.L.; Jikich, S.A.; LaCount, R.B.; DuBose, S.B.; Ozdermir, E.; Morsi, B.I.; Schroeder, K.T. Sequestration of carbon dioxide in coal with enhanced coalbed methane reservoirs—A review. *Energy Fuels* **2005**, *19*, 659–724. [CrossRef]
52. Myers, A.L.; Monson, P.A. Adsorption in porous materials at high pressure: Theory and experiment. *Langmuir* **2002**, *18*, 10261–10273. [CrossRef]
53. Zhang, T.; Ellis, G.S.; Ruppel, S.C.; Milliken, K.; Yang, R. Effect of organicmatter type and thermal maturity on methane adsorption in shale-gas systems. *Org. Geochem.* **2012**, *47*, 120–131. [CrossRef]
54. Rouquerol, J.; Avnir, D.; Fairbridge, C.W.; Everett, D.H.; Haynes, J.H.; Pernicone, N.; Ramsay, J.D.F.; Sing, K.S.W.; Unger, K.K. Physical chemistry Division Commission on Colloid and Surface Chemistry, Subcommittee on Characterization of Porous Solids: Recommendations for the characterization of porous solids. *Pure Appl. Chem.* **1994**, *66*, 1739–1758. [CrossRef]
55. Sui, H.; Yao, J. Molecular simulation of CO_2/CH_4 competitive adsorption in kerogen. *J. China Univ. Pet.* **2016**, *40*, 147–154.
56. Sircar, S. Estimation of isosteric heats of adsorption of single gas and multicomponent gas mixtures. *Ind. Eng. Chem. Res.* **1992**, *31*, 1813–1819. [CrossRef]
57. Ji, L.; Zhang, T.; Milliken, K.L.; Qu, J.; Zhang, X. Experimental investigation of main controls to methane adsorption in clay-rich rocks. *Appl. Geochem.* **2012**, *27*, 2533–2545. [CrossRef]
58. Ziemiański, P.P.; Derkowski, A.; Szczurowski, J.; Kozieł, M. The structural versus textural control on the methane sorption capacity of clay minerals. *Int. J. Coal Geol.* **2020**, *224*, 103483. [CrossRef]
59. Chalmers, G.R.L.; Bustin, R.M.; Ian, P.M. Characterization of gas shale pore systems by porosimetry, pycnometry, surface area, and field emission scanning electron microscopy/transmission electron microscopy image analyses: Examples from the Barnett, Woodford, Haynesville, Marcellus, and Doig units. *AAPG Bull.* **2012**, *96*, 1099–1119.
60. Sing, K.S.W.; Everett, D.H.; Haul, R.A.W.; Moscou, L.; Pierotti, R.A.; Rouquerol, J.; Siemieniewska, T. Reporting physisorption data for gas/sold systems with special reference to the determination of surface area and porosity. *Pure Appl. Chem.* **1985**, *57*, 603–619. [CrossRef]
61. Mosher, K.; He, J.; Liu, Y.; Rupp, E.; Wilcox, J. Molecular simulation of methane adsorption in micro- and mesoporous carbons with applications to coal and gas shale systems. *Int. J. Coal Geol.* **2013**, *109–110*, 36–44. [CrossRef]
62. Zhou, S.; Wang, H.; Xue, H.; Guo, W.; Li, X. Supercritical methane adsorption on shale gas: Mechanism and model. *China Sci. Bull.* **2017**, *62*, 4189–4200. [CrossRef]
63. Gasparik, M.; Betier, P.; Gensterblum, Y.; Ghanizadeh, A.; Krooss, B.M.; Littke, R. Geological controls on the methane storage capacity in organic-rich shales. *Int. J. Coal Geol.* **2014**, *123*, 34–51. [CrossRef]
64. Wang, L.; Li, C.; Shi, Y.; Wang, Y. Distributions of geotemperature and terrestrial heat flow density in Lower Yangtze area. *Acta Geogr. Sin.* **1995**, *38*, 469–476.
65. Hu, D.; Zhang, H.; Ni, K.; Yu, G. Main controlling factors for gas preservation conditions of marine shales in southeastern margins of the Sichuan Basin. *Nat. Gas Ind.* **2014**, *34*, 17–23.
66. Liu, H.; Wang, H. Ultra-low water saturation characteristics and the identification of over-pressured play fairways of marine shales in south China. *Nat. Gas Ind.* **2013**, *33*, 140–144.
67. Wei, Z.; Wei, X. Comparison of gas-bearing property between different pore types of shale: A case from the Upper Ordovician Wufeng and Longmaxi Fms in the Jiaoshiba area, Sichuan Basin. *Nat. Gas Ind.* **2014**, *34*, 37–41.
68. Huang, L.; Ning, Z.; Wang, Q.; Zhang, W.; Cheng, Z.; Wu, X.; Qin, H. Effect of organic type and moisture on CO_2/CH_4 competitive adsorption in kerogen with implications for CO_2 sequestration and enhanced CH_4 recovery. *Appl. Energy* **2018**, *210*, 28–43. [CrossRef]
69. Li, W.; Stevens, L.A.; Uguna, C.N.; Vane, C.H.; Meredith, W.; Tang, L.; Li, Q.; Snape, C.E. Comparison of the impact of moisture on methane adsorption and nanoporosity for over mature shales and their kerogens. *Int. J. Coal Geol.* **2021**, *237*, 103705. [CrossRef]
70. Setzmann, U.; Wagner, W. A new equation of state and tables of thermodynamic properties for methane covering the range from the melting line to 625 K at pressures up to 100 MPa. *J. Phys. Chem. Ref. Data* **1991**, *20*, 1061. [CrossRef]
71. Li, Y.; Liu, H.; Zhang, L.; Lu, Z.; Li, Q.; Huang, Y. Lower limits of evaluation parameters for the lower Paleozoic Longmaxi shale gas in southern Sichuan Province. *Sci. China Earth Sci.* **2013**, *56*, 710–717. [CrossRef]